DC–DC Converter Based Photovoltaic Simulator With a Double Current Mode Controller

Weichao Zhang and Jonathan W. Kimball , *Senior Member, IEEE*

Abstract—This paper explores the performance of a dc–dc converter, which emulates the output characteristics of a real photovoltaic (PV) module. The PV simulator uses a double current mode controller to ensure fast and accurate reproduction of a module's current-voltage (IV) characteristics. A portable PV simulator prototype of 85 W is examined in terms of its steady state IV curve matching capacity and the convergence time corresponding to step changes in current source load, voltage source load, and insolation levels. The IV characteristics of the PV module are implemented as a look-up-table, which determines the reference output current from measured output voltage. The Thevenin equivalent circuit of the PV module is used to model its small-signal (linearized) characteristics for stability analysis. Extensive simulation and experimental results, with loads that have current-source, voltage-source, and resistive characteristics, validate the converter's suitability for replacing a PV module in most laboratory situations. Modularity and compatibility with a maximum power point tracker have also been validated.

Index Terms—Digital control, photovoltaic (PV) simulator, predictive current mode control, solar panel current-voltage (IV) curve.

I. INTRODUCTION

SOLAR energy has experienced phenomenal growth in recent years due to both technological improvements resulting in cost reductions and government policies supportive of renewable energy development and utilization. The most common way to harness solar energy is by converting it to electrical energy using photovoltaic (PV) modules. One challenge when interfacing devices to PV modules is that PV modules behave like a current source at high output current and a voltage source at low output current. This special output characteristic of PV modules requires devices that interface with them to have maximum power point tracking (MPPT) capabilities in order to maximize the efficiency of PV modules [1], [2]. Field testing MPPT converters with real PV modules is challenging. First, PV modules are still expensive despite the fact that their price

has been on a steady decline over the past decade. Installation of PV modules is also an expensive and time-consuming process. Second, the output of PV modules is dependent on the insolation level and temperature, which varies depending on the time of year and weather of the day; hence test conditions cannot be controlled and repeatable test results cannot be obtained.

PV systems are unusual in that they cannot be turned ON or OFF. That is, they produce voltage, possibly at dangerous levels, any time they are receiving sunlight. In addition, PV panels generate dc voltage, which is not commonly used by electricians in their normal work. Because of the current limiting properties of PV cells, they are incapable of producing sufficient fault currents to operate over-current protection devices such as fuses [3], [4]. Therefore, PV installation requires different certifications.

An alternative to field testing a PV system is to replace the PV module with a PV simulator, which is a device that has the same output characteristic of a real PV module but that can be used within a laboratory environment at any time of the year. The method used in this paper to simulate a real PV module is to digitally implement the current-voltage (IV) characteristic of a PV module through a look-up-table (LUT) that resides in the memory of the microcontroller and convert the digital signal to power output though a dc–dc converter [5]–[9]. The major advantage of digitally implemented PV simulators is that users can set conditions such as temperature and insolation level, or even change which type of module is being simulated. Moreover, digital control of a pulse-width modulation (PWM) converter has the advantage of high noise immunity, immunity to analog component variations, fast design process, and programmability for multiple applications, as compared to an analog counterpart [10]–[12]. With digital control, more complex control schemes can be easily achieved, such as the double current mode controller described in the present work.

This work extends previous work [13] and uses a similar framework. However, the method in [13] was only demonstrated with resistive loads. When tested on other types of loads, with current-source and voltage-source behavior, the converter became unstable. Therefore, a new approach was proposed in [14] and extended here to include output impedance analysis. The inner loop uses predictive current mode, which is a fast, stable control method.

In Section II, the converter is described and the mathematical model of a PV module is derived; two methods to implement the mathematical model as a LUT are proposed. In Section III, the small signal transfer functions are derived, and the inner

W. Chang was with the Department of Electrical and Computer Engineering, Missouri University of Science and Technology, Rolla, MO 65409 USA. He is now with AT&T, Tustin, CA 92782 USA (e-mail: wzrz9@mst.edu).

J. W. Kimball is with the Department of Electrical and Computer Engineering, Missouri University of Science and Technology, Rolla, MO 65409 USA (e-mail: kimballjw@mst.edu).
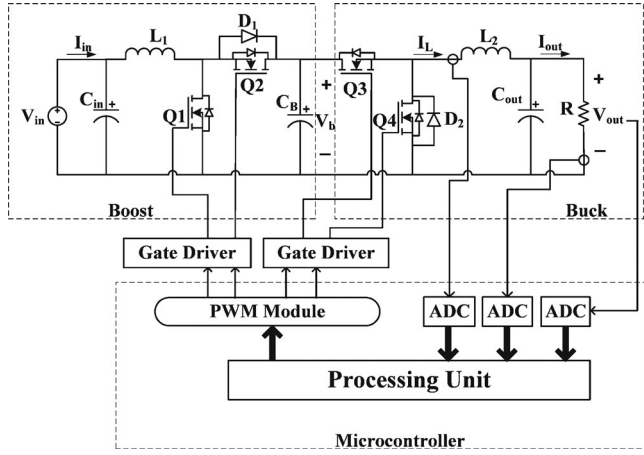
Fig. 1. System configuration of PV Simulator.

Fig. 2. Equivalent circuit of a PV cell.

a peak-to-peak ripple voltage of 50 mV. As long as the filter capacitor C2 is relatively large, the ripple from the first stage boost converter can be ignored and has no effect on the output ripple of the second stage buck converter.

predictive current mode controller and the outer PI controller are designed to satisfy gain margin and phase margin requirements. Section IV includes both simulation results and experimental results that verify the operation of the controller.

II. System Configuration

A. Power Stage

Fig. 1 shows the system configuration for a dc–dc based PV simulator that comprises a step-up synchronous boost converter and a step-down synchronous buck converter. V_{in} represents a dc source of 15 V. To facilitate portability, a wide range of input sources is allowed, including a bench supply or a battery. The boost converter outputs a standard voltage of 30 V. The buck converter has an output voltage range of 0–30 V from a standard input voltage of 30 V. One major advantage of using a synchronous topology is high efficiency, which is essential for portable applications. Another major advantage of using a synchronous topology here is that the dc–dc converter will never enter discontinuous conduction mode (DCM). This allows us for a much simpler controller implementation since there is never a transition between continuous conduction mode and DCM. However, with a synchronous topology, the number of MOSFETs used is increased from two to four. Dead-bands also must be introduced between S1 and S2, and between S3 and S4 to prevent cross conduction. The inductor and the capacitor for the second stage buck converter are calculated according to the standard design equations

$$L = \frac{V_{\mathrm{in}}}{4 \Delta I_{\mathrm{pp}} f_{\mathrm{sw}}} \tag{1}$$

$$\Delta V_{\mathrm{out}} = R_{\mathrm{ESR}} \Delta L + \frac{\Delta L}{8 C_{\mathrm{out}} f_{\mathrm{sw}}} \tag{2}$$

$$C \geq \frac{\Delta I_{\mathrm{pp}}}{8 f_{\mathrm{sw}} \Delta V_{\mathrm{pp}}}. \tag{3}$$

In order to satisfy current ripple and voltage ripple requirements in the worst case scenario, the inductor and capacitor values were chosen for a peak-to-peak ripple current of 1 A and
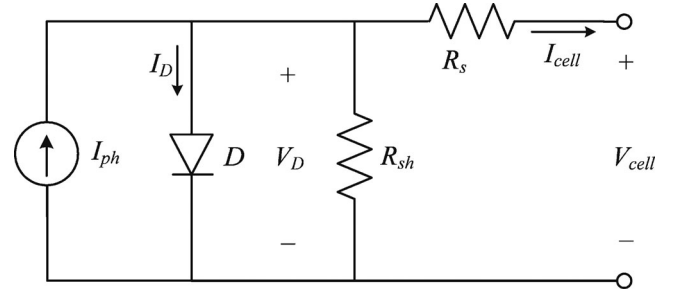
B. Microcontroller

The microcontroller chosen is the 32-bit TMS320F28335 by Texas Instruments, Dallas, TX, USA. The microcontroller runs at 150 MHz and has a built-in floating-point-unit, 16 channels of 12-bit ADCs, and six PWM modules. The DSP is required to have three ADC channels, four PWM output channels, built-in or external random access memory (RAM), and a processing unit, preferably with floating point math capability. The ADCs are used to measure the output voltage, output current, and the buck converter inductor current, as needed by the double current mode controller. The PWM signals for the two switching pairs S1/S2 and S3/S4 must be generated with deadband to prevent cross-conduction, which is easily achieved by properly configuring the ePWM modules within the microcontroller.

C. PV Module Modeling

PV generators are neither constant voltage sources nor current sources but can be approximated as current generators with dependent voltage sources. Fig. 2 shows an equivalent circuit of a PV cell. A single PV cell is considered along with a current source, a diode, a shunt resistor, and a series resistor. The diode equation is given as I_{out}

$$I_D = I_0 \left(e^{\frac{V_D}{n V_t}} - 1 \right) \tag{4}$$

$$V_t = \frac{AKT}{q} \tag{5}$$

where
I_D is the current the diode;
V_D is the voltage the diode;
I_0 is the reverse saturation current;
A   is the ideality factor;
K   is the Boltzmann's constant;
T   is the absolute temperature;
q   is the elementary charge.

A PV module consists of many series-connected PV cells, hence the voltage across each cell is the total output voltage of the PV module divided by the number of series-connected cells.
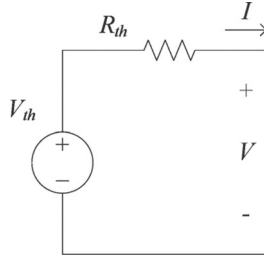
Fig. 3.   Thevenin equivalent circuit.

The output equation that relates the output current and output voltage of a PV module can be derived as

$$I_{\text{out}} = I_{\text{ph}} - I_0 \left(e^{\frac{V_{\text{out}} + I_{\text{out}} R_s}{N V_t}} - 1 \right) - \frac{V_{\text{out}} + I_{\text{out}} R_s}{R_{\text{sh}}}. \quad (6)$$

The IV curve of a PV module is affected by temperature, insolation level, which determines the short circuit current, shunt resistance, and series resistance. By varying the parameters in (6), one can model many different kinds of PV modules under different environmental conditions.

D. Thevenin Equivalent Circuit Derivation

The PV module IV characteristic is represented by a LUT, which is a physical memory block inside of the microcontroller. In order to store the IV curve as a lookup-table in the memory of the DSP, a Thevenin equivalent circuit shown in Fig. 3 is derived. Thevenin equivalent voltage V_{th} and resistance R_{th} are depend on the operating conditions such as insolation and the load. When the insolation level and/or the load change, the linear IV characteristics change as well.

In order to obtain the linear characteristics curves, the differentiated equation with respect to V of (6) is given as

$$\frac{dI}{dV} = -I_0 \frac{1 + R_s \frac{dI}{dV}}{N A V_t} e^{\frac{V + I R_s}{A V_t}} - \frac{1 + R_s \frac{dI}{dV}}{R_{\text{sh}}}. \quad (7)$$

The Thevenin resistance, R_{th}, is the slope and can be derived as

$$-R_{\text{th}} = -R_s - \left(\frac{I_0}{A V_t} e^{\frac{V + I R_s}{A V_t}} + \frac{1}{R_{\text{sh}}} \right)^{-1}. \quad (8)$$

According to maximum power transfer theorem, combining (7) and (8), the maximum power point load line is

$$\frac{V}{I} = R_s + \left(\frac{I_0}{A V_t} e^{\frac{V + I R_s}{A V_t}} + \frac{1}{R_{\text{sh}}} \right)^{-1}. \quad (9)$$

The LUT is a 1000-element, one-dimensional array that stores the output currents corresponding to output voltages. Here the size of the array is limited by the RAM size of the microcontroller and can be increased if higher resolution is necessary and RAM permits. The LUT is updated whenever the controller receives a command to change the operating conditions, such as a different insolation level. With a set number of matching output voltage and output current from PV module, a collection of linear characteristics is obtained in Simulink,[1] as shown in Fig. 4. Each tangent line corresponding to a different load

[1]MATLAB and Simulink are registered trademarks of The MathWorks, Inc.
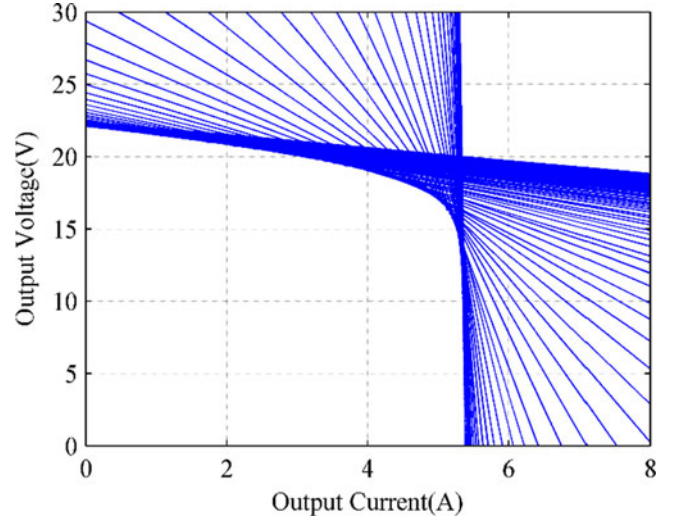

Fig. 4.   Linearized IV curve under 100% insolation.
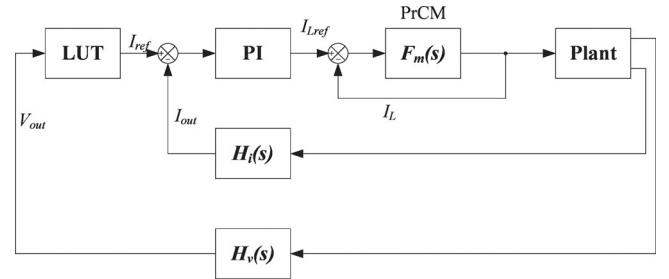

Fig. 5.   Control block diagram of the PV simulator.

on the IV curve under a 100% insolation condition. The maximum power point (MPP) is reached when the absolute value of the slope equals the load resistance. The nonlinear IV curve is formed by the intersection of the linear IV curve and the load line. This point is determined by different load resistance and its corresponding slope.

III. Controller Implementation

With the first-stage boost converter running open loop, all control efforts are focused on the second-stage buck converter. The control block diagram is shown in Fig. 5. In order to design a controller for the simulator, the small signal transfer functions of the second-stage buck converter must be derived. The complete small-signal model is illustrated in Fig. 6. These small signal transfer functions can be derived using averaged switch modeling or state space averaging; both methods produce the same transfer functions. The model includes the inductor dc resistance and equivalent series resistance (ESR) of the capacitor. Assuming a pure resistive load and the inductor dc resistance and the ESR of the capacitor is much less than the load resistance, the small signal transfer functions are derived as (10)–(12) shown at the bottom of the next page, where

$G_{vd(s)}$ is the small signal transfer function from duty cycle to output voltage;

$G_{id(s)}$ is the small signal transfer function from duty cycle to inductor current; and
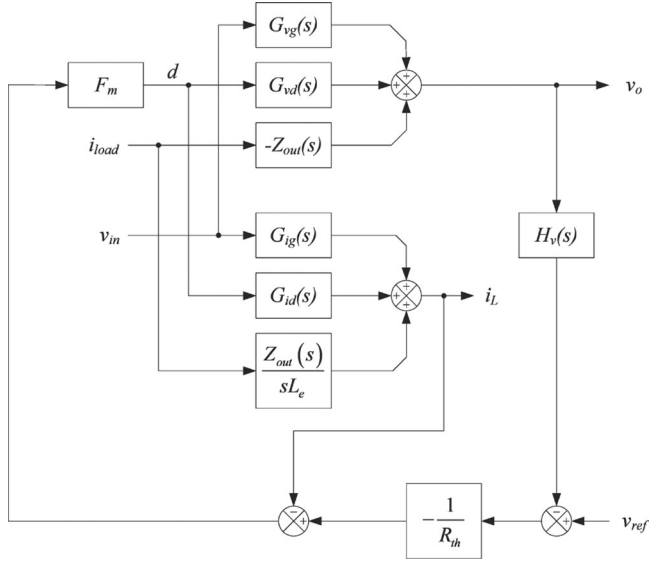
Fig. 6. Mathematical building block of the converter operating in current mode control.

$G_{iv(s)}$ is the small signal transfer function from output voltage to output current, which depends on the load.

Using the bilinear transform, the discrete time equivalent of (10)–(12) can be determined numerically from

$$G_{vd(z)} = G_{vd(s)}\big|_{s=\frac{2(z-1)}{T_s(z+1)}} \tag{13}$$

$$G_{id(z)} = G_{id(s)}\big|_{s=\frac{2(z-1)}{T_s(z+1)}} \tag{14}$$

$$G_{iv(z)} = G_{iv(s)}\big|_{s=\frac{2(z-1)}{T_s(z+1)}}. \tag{15}$$

A. Inner Current Mode Control

Predictive current control [15], [16] is an accurate digital control technique that is based on inductor current predicted by sampled inductor current and output voltage. The essential concept is to choose the duty ratio that will exactly achieve the desired inductor current at the next sample time. There are three kinds of predictive current mode controls – peak current control, average current control, and valley current control; and there are four kinds of modulation methods – trailing edge, leading edge, trailing triangle, and leading triangle. Each of the

three current control methods must be paired with the correct modulation method in order to be stable over the whole range of the duty ratio. The buck converter's duty ratio range is [0,1], so the current control method must be paired with the right modulation method. Here average current control is used to increase noise immunity, and is paired with trailing triangle modulation to give stability over the whole duty ratio range of the buck converter. The predictive current mode control law for a buck converter is

$$d[n+1] = -d[n] + \frac{L}{V_{\text{in}}T_s}\left(i_{\text{ref}}[n] - i_L[n]\right) + \frac{2V_{\text{out}}}{V_{\text{in}}}. \tag{16}$$

The small signal discrete time transfer function from current error to duty ratio is

$$d_{(z)} = F_{m(z)}\left(i_{\text{ref}(z)} - i_{L(z)}\right) \tag{17}$$

where

$$F_{m(z)} = \frac{L}{V_{\text{in}}T_s}\cdot\frac{1}{z+1}. \tag{18}$$

The small-signal gain of this inner loop is used in determining other gains, but the actual implementation uses (16).

B. Outer Current Mode PI Controller

The compensator is designed based on the common PI controller as

$$PI = K_p + \frac{K_I}{s} = \frac{K_P\left(s + \frac{K_I}{K_P}\right)}{s}. \tag{19}$$

The small signal transfer functions of the buck converter are dependent on the load condition. In order to avoid having to implement mode switching or gain scheduling in the controller, it is necessary to find the load conditions that place the most stringent requirements on the PI controller. If the load resistance is assumed to be between 20 and 200 Ω, then a PI controller can be designed to satisfy both load conditions. Using MATLAB (see note 1 at the bottom of the page 3), a range of operating conditions can be considered so that a PI controller can be produced to satisfy the requirements of phase margin greater than 75° and gain margin greater than 6 dB. The zero of the PI controller is determined primarily by the light load condition, while the gain is determined primarily by the heavy load condition. Considering both, a stable controller may be found for the entire

$$
\begin{aligned}
G_{\text{vd}(s)} &= \frac{V_{\text{out}(s)}}{d(s)}\big|_{V_{\text{in}(s)}=0} = \frac{V_{\text{in}}R\left(1 + CR_{\text{esr}}s\right)}{LC\left(R + R_{\text{esr}}\right)s^2 + \left[L + CR_{\text{esr}}R_L + CR\left(R_{\text{esr}} + R_L\right)\right]s + R + R_L} \\
&\approx \frac{V_{in}R\left(1 + CR_{\text{esr}}s\right)}{LCRs^2 + \left[L + CR\left(R_{\text{esr}} + R_L\right)\right]s + R + R_L} \tag{10}
\end{aligned}
$$

$$
\begin{aligned}
G_{id(s)} &= \frac{i_{L(s)}}{d(s)}\big|_{V_{\text{in}(s)}=0} = \frac{V_{\text{in}}\left[1 + C\left(R_{\text{esr}} + R\right)s\right]}{LC\left(R + R_{\text{esr}}\right)s^2 + \left(L + CR_{\text{esr}}R_L + CR\left(R_{\text{esr}} + R_L\right)\right)s + R + R_L} \\
&\approx \frac{V_{\text{in}}\left(1 + CRs\right)}{LCRs^2 + \left(L + CR\left(R_{\text{esr}} + R_L\right)\right)s + R + R_L} \tag{11}
\end{aligned}
$$

$$G_{iv(s)} = \frac{I_{\text{out}(s)}}{V_{\text{out}(s)}} = \frac{1}{R} \tag{12}$$

TABLE I
PV MODULE AND CIRCUIT PARAMETERS

Switching Frequency (f_{sw})	100 kHz
Inductor (L_1)	138 μH
Inductor (L_2)	138 μH
Capacitor (C_1)	560 μF
Capacitor (C_2)	560 μF
Capacitor (C_3)	560 μF
Short Circuit Current (I_{sc})	5.4 A
Open Circuit Voltage (V_{oc})	22 V
Internal Series Resistance (R_s)	364 mΩ
Internal Shunt Resistance (R_{sh})	1.21 kΩ
Ideality Factor (A)	0.6125

operating range. The PI controller is chosen to be

$$G_{c(s)} = \frac{2500\,(1 + 0.0065\,s)}{s}. \tag{20}$$

The discrete time equivalent of $G_{c(s)}$ is derived as

$$G_{c(z)} = G_{c(s)}\big|_{s = \frac{2(z-1)}{T_s(z+1)}} = \frac{5.23z - 6.59}{z - 1} \tag{21}$$

and implemented in the microcontroller.

C. Current Mode Controller Converter

Fig. 5 illustrates the small-signal block diagram of the current mode controlled converter. The current modulator employed here is discussed in detail in [7]. The extra elements in this control scheme are R_{th} and F_m. The term R_{th} represents the current sensing resistor that transforms current to voltage to sense the inductor current. The term F_m represents gain blocks related to the inner predictive current modulator. The system of equations yields in the closed-loop input impedance

$$Z_{\text{in}}(s) = \frac{V_{\text{in}}(s)}{I_{\text{in}}(s)}\bigg|_{I_{\text{load}}(s)=0} \tag{22}$$

$$Z_{\text{in}}(s) = \frac{-\left(1 + HF_m G_{vd} + F_m\left(G_{vd} + G_{id}\right)\right)}{G_{ig}\left(\left(\frac{F_m G_{id}}{G_{ig}} - 1\right) + F_m\left(\frac{HG_{vg}}{G_{ig}} + \frac{1 + G_{vg}}{G_{ig}}\right)\right)}. \tag{23}$$

If V_{ref} and V_g are set to zero, this system of equations yields in the closed-loop output impedance

$$Z_{\text{out}}(s) = \frac{V_{\text{out}}(s)}{-I_{\text{load}}(s)}\bigg|_{V_g(s)=0} \tag{24}$$

$$Z_{\text{out}}(s) = \frac{F_m H(s)\left(G_{vd}(s) + G_{id}(s)\right)}{F_m H(s)\left(G_{vd}(s) + G_{id}(s)\right) - R_{th}}. \tag{25}$$

IV. SIMULATIONS AND EXPERIMENTAL RESULTS

The PV simulator (see Fig. 1) has been built with the circuit specification shown in Table I. This section discusses the performance of PV simulator with voltage-source load and current-source load. The PV simulator is set to simulate the multicrystalline PV module model SW-S85P from SunWize.
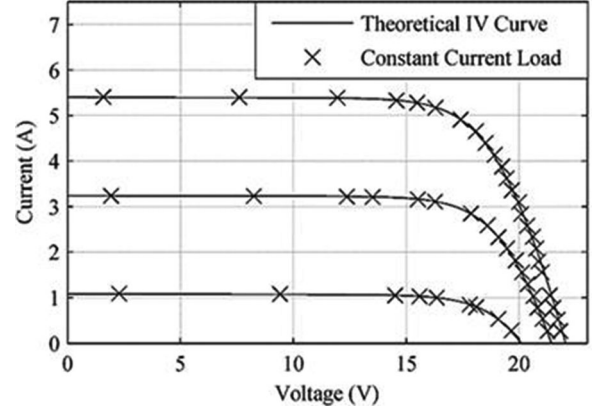

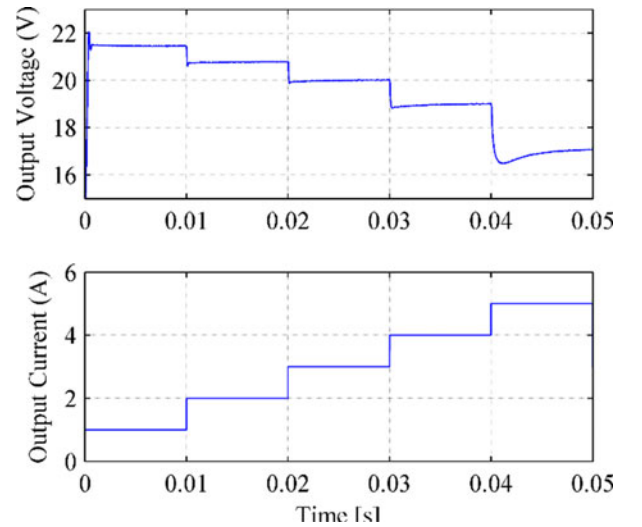Fig. 7. PV simulator response with constant current load (experimental).

Fig. 8. Computer simulated output waveforms of the PV simulator when current source changes from 1 to 5 A.

The simulation results presented in this section are carried out in MATLAB/Simulink with PLECS.[2]

First, the steady state performance was verified against the desired IV characteristic. Fig. 7 illustrates the experimental performance for 100%, 60%, and 20% insolation and a varying current-source load. The experimental data lie on the commanded IV curves precisely, as expected.

Next, transient behavior was verified in MATLAB/Simulink with PLECS. Figs. 8 and 9 show the performance of the PV simulator under current source step and voltage source step. In addition to following the commanded IV curves in steady state, convergence to a new operating point after the load changes is fast and stable. Some variation is observed depending on the load type and operating point, but the converter is stable throughout. Figs. 10 and 11 show the insolation step response of the PV simulator with current source load and voltage source load, respectively. The insolation is initially 100% and it drops

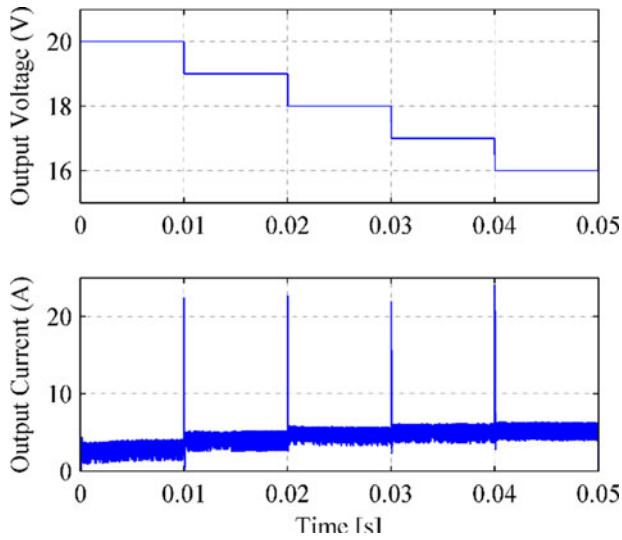[2]PLECS is a registered trademark of Plexim GmbH.

Fig. 9. Computer simulated output waveforms of the PV simulator when voltage source changes from 20 to 16 V.
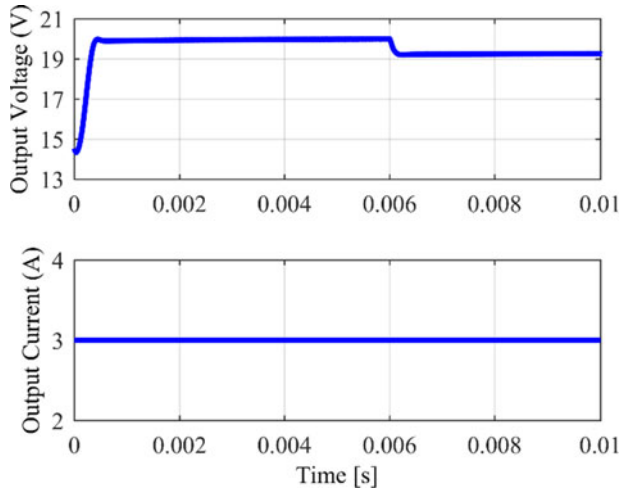

Fig. 10. Computer simulated insolation step change from 100% to 80% with current source load.
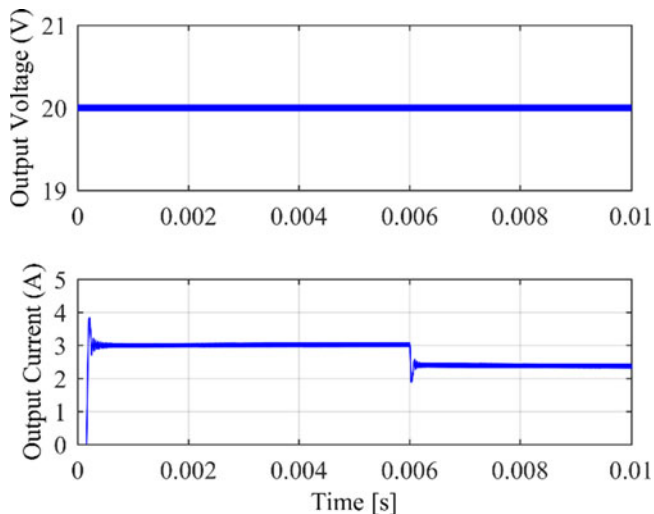

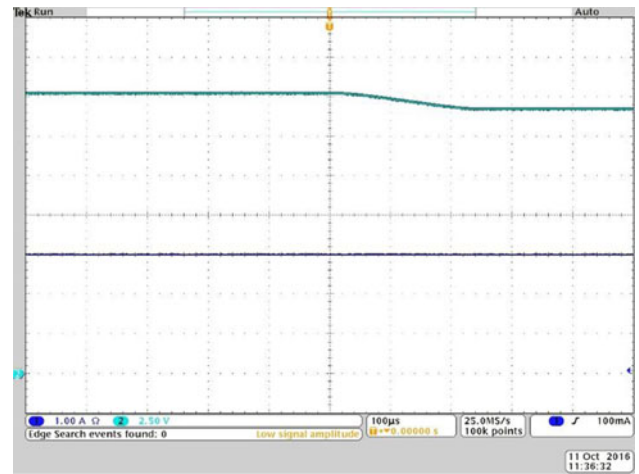Fig. 11. Computer simulated insolation step change from 100% to 80% with voltage source load.

Fig. 12. Experimental insolation step change from 100% to 80% with current source load = 3 A. Upper trace: voltage, 2.5 V/div; lower trace: current, 1.0 A/div; 100 μs/div.
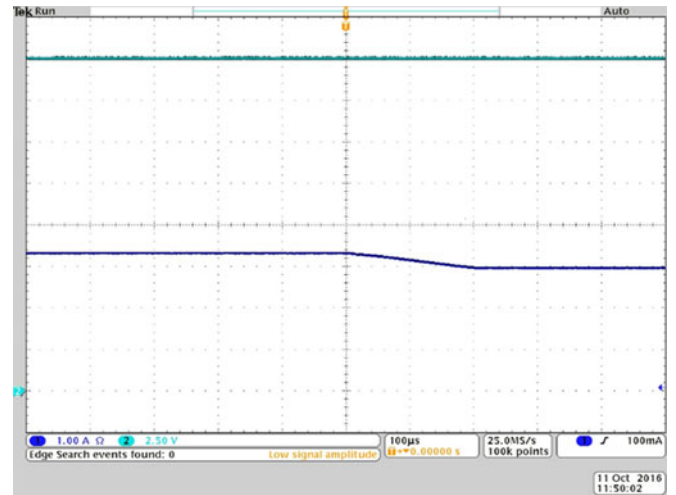

Fig. 13. Experimental insolation step change from 100% to 80% with voltage source load = 20 V. Upper trace: voltage, 2.5 V/div; lower trace: current, 1.0 A/div; 100 μs/div.
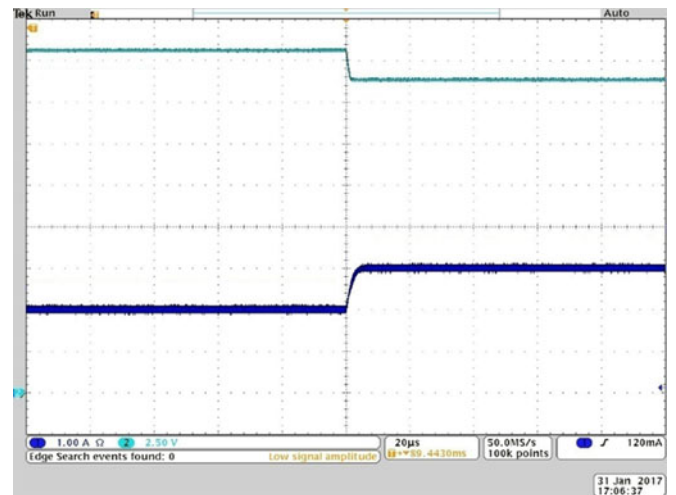

Fig. 14. Experimental output waveforms of the PV simulator when current source changes from 2 to 3 A. Upper trace: voltage, 2.5 V/div; lower trace: current, 1.0 A/div; 20 ms/div.
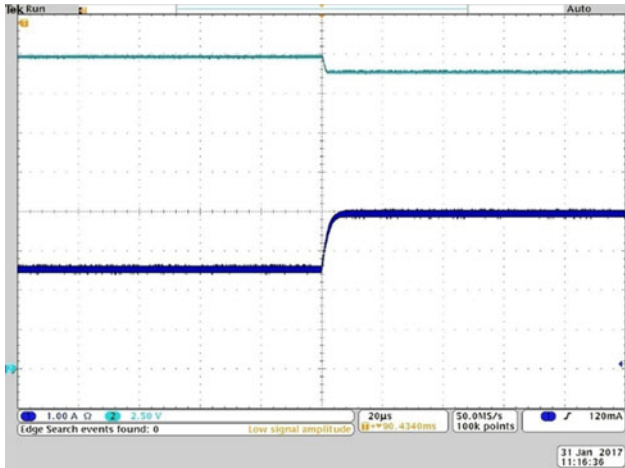
Fig. 15. Experimental output waveforms of the PV simulator when voltage source changes from 20 to 19 V. Upper trace: voltage, 2.5 V/div; lower trace: current, 1.0 μs/div; 20 μs/div.
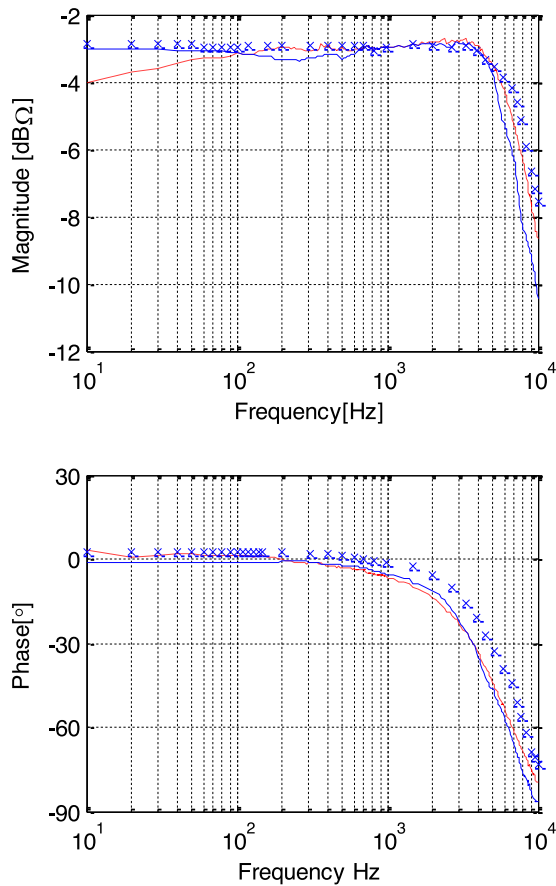

Fig. 16. Theoretical, modeling, and measured closed-loop output impedances of buck converter in current source load. The red dashed line traces show the simulation results, the *x* line traces show the modeling output impedance, and the blue solid traces show the measured impedance.
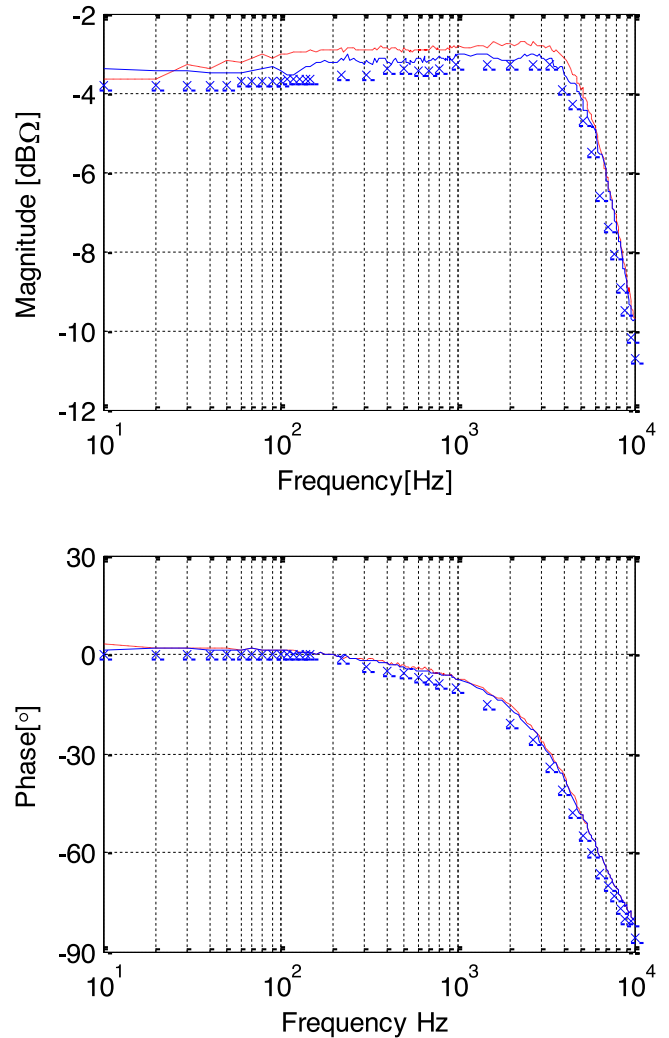

Fig. 17. Theoretical, modeling, and measured closed-loop output impedances of buck converter in voltage source load. The red dashed line traces show the simulation results, the *x* line traces show the modeling output impedance, and the blue solid traces show the measured impedance.

perturbations: insolation steps with current-source and voltage-source loads, load steps with current-source and voltage-source loads. The time scales have been adjusted to more completely illustrate the behavior.

Next, output impedance was measured. Figs. 16 and 17 illustrate a combination of theoretical, simulation, and experimental results. The theoretical curves were derived from (25). The simulation curves used the frequency sweeping capabilities of the PLECS Blockset. The experimental curves were obtained using a Venable Model 350B/5060A frequency response analyzer. In each figure, the blue continuous line traces show the show the measured impedance, the x line traces show the modeling output impedance, and the red dashed line traces show the simulation results.

A significant advantage of the PV simulator is the ability to explore different panel connections and performance of PV-connected converters, such as a maximum power point tracker (MPPT). Two similar, but slightly different, simulators were
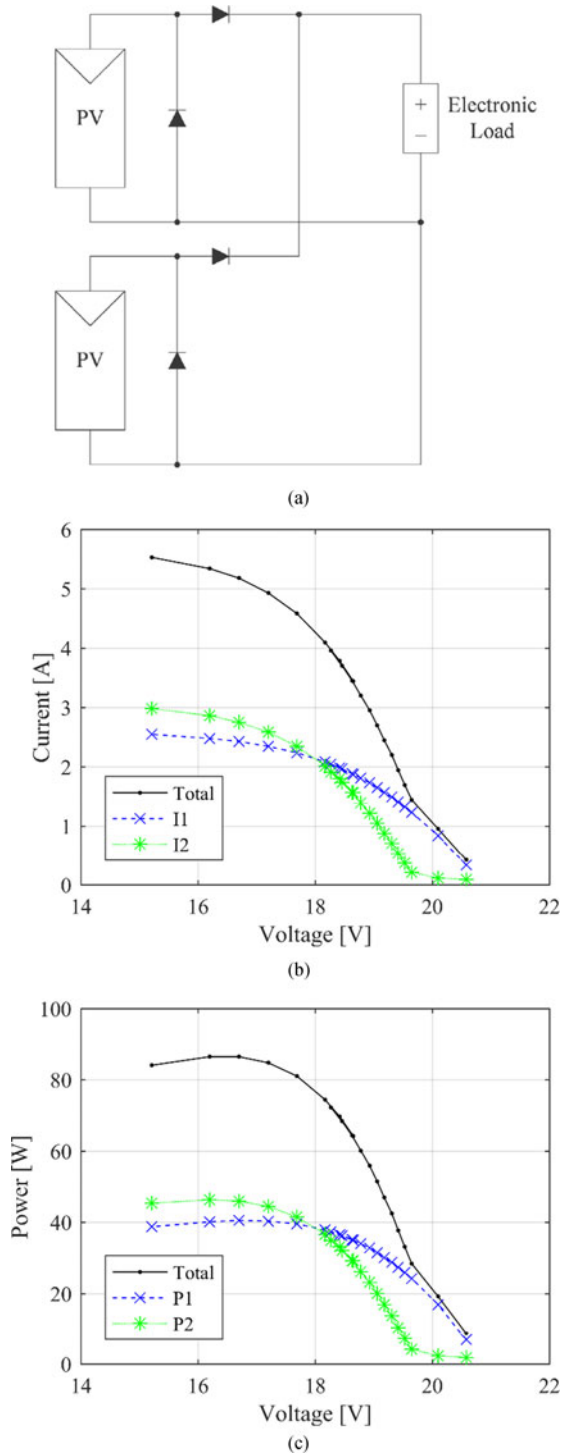
to 80%. Again, convergence to the new operating point is fast and stable, regardless of the load type.

The transient behavior was also verified experimentally. Figs. 12–15 show the experimental results for a variety of

Fig. 18.   Parallel connected PV simulators. (a) Schematic. (b) Current. (c) Power.

Fig. 19.   Series connected PV simulators. (a) Schematic. (b) Current. (c) Power.

connected in parallel and in series, as shown in Figs. 18 and 19. The total array-level output matches expectations, and the different panel contributions are visible. For example, in the parallel connection, when the voltage is low enough for both panels to contribute, an increase in current is observed. Similarly, in the ser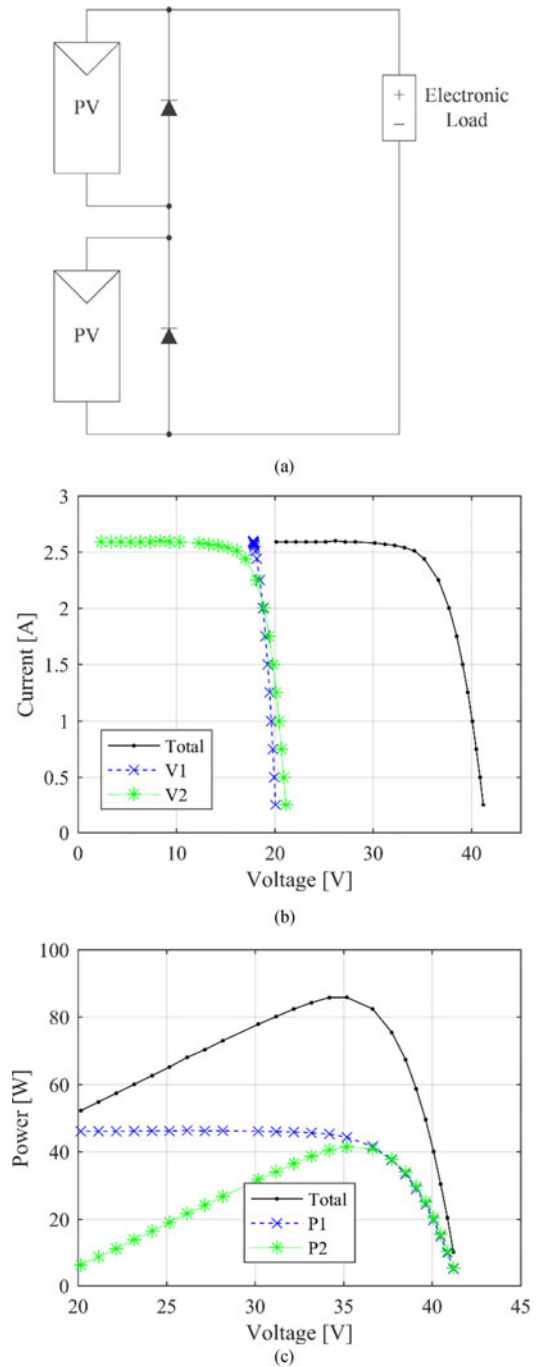ies connection, one panel enters constant-current mode earlier than the other, thereby limiting the possible power output. The parallel-connected panels were used to power an MPPT, in place of the electronic load indicated in Fig. 18(a). The MPPT is able to accurately track the maximum power point using a conventional perturb and observe algorithm, as shown in Fig. 20. The large voltage swing is caused by limited resolution on the MPPT controller, and is expected. The waveforms in Fig. 20 illustrate that the simulator behaves like a true PV panel.
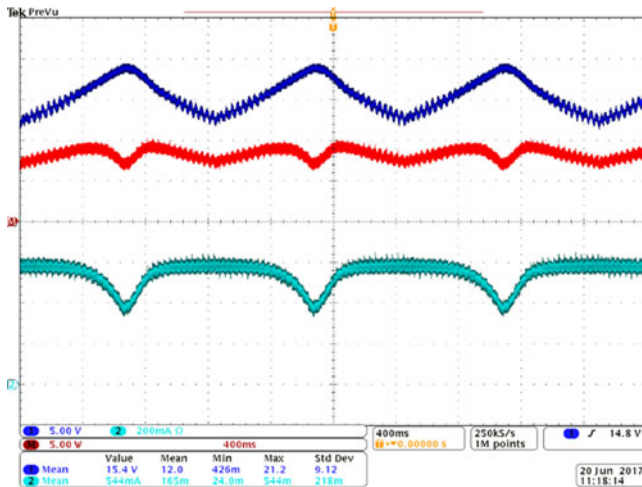
Fig. 20.   Experiment with parallel-connected panels of Fig. 18(a) connected to a maximum power point tracker; top trace, panel voltage, 5 V/div; middle trace, computed power, 5 W/div; bottom trace, panel current, 0.2 A/div.

V. CONCLUSION

A dc–dc converter based PV simulator with double current controller is presented in this paper. Simulation results showed that the PV simulator can work with different types of loads with predicable IV characteristics. The IV characteristic of the PV module of interest is implemented as LUT that resides in the RAM of the DSP. A double current mode controller that consists of an outer PI controller and an inner predictive current mode controller is used to regulate the output current and output voltage to the match the LUT data. With a double current mode controller, the stability of the system is guaranteed over a wide range of load conditions. A portable 85-W PV simulator proto-type was built to demonstrate the effectiveness of the presented method. In future work, the dynamics will be explored in more detail and compared against real PV modules.

ACKNOWLEDGMENT

REFERENCES

[1] J. W. Kimball and P. T. Krein, "Discrete-time ripple correlation control for maximum power point tracking," *IEEE Trans. Power Electron.*, vol. 23, no. 5, pp. 2353–2362, Sep. 2008.

[2] T. Esram and P. L. Chapman, "Comparison of photovoltaic array maximum power point tracking techniques," *IEEE Trans. Energy Convers.*, vol. 22, no. 2, pp. 439–449, Jun. 2007.

[3] H. Nagayoshi, "Characterization of the module/array simulator using I-V magnifier circuit of a pn photo-sensor " in *Proc. 3rd World Conf. Photovolt. Energy Convers.*, 2003, vol. 2, pp. 2023–2026.

[4] A. Koran, K. Sano, R. Y. Kim, and J. S. Lai, "Design of a photovoltaic simulator with a novel reference signal generator and two-stage LC out-put filter," *IEEE Trans. Power Electron.*, vol. 25, no. 5, pp. 1331–1338, May 2010.

[5] M. L. Orozco-Gutierrez, J. M. Ramirez-Scarpetta, G. Spagnuolo, and C. A. Ramos-Paja, "A technique for mismatched PV array simulation," *Renew. Energy*, vol. 55, pp. 417–427, Jul. 2013.

[6] G. Vachtsevanos and K. Kalaitzakis, "A hybrid photovoltaic simulator for utility interactive studies," *IEEE Trans. Energy Conversion*, vol. EC-2, pp. 227–231, Jun. 1987.

[7] E. Koutroulis, K. Kalaitzakis, and V. Tzitzilonis, "Development of a FPGA-based system for real-time simulation of photovoltaic mod-ules," in *Proc. 17th Int. Workshop IEEE Rapid Syst. Prototyping*, 2006, pp. 200–206.

[8] H. Lee, M. J. Lee, S. N. Lee, H. C. Lee, H. K. Nam, and S. J. Park, "Development of photovoltaic simulator based on DC-DC converter," in *Proc. 2009 31st Int. Conf. Telecommun. Energy*, 2009, pp. 1–5.

[9] J. P. Lee *et al.*, "Development of a photovoltaic simulator with novel simulation method of photovoltaic characteristics," in *Proc. 2009 31st Int. Conf. Telecommun. Energy*, 2009, pp. 1–5.

[10] E. Koutroulis and F. Blaabjerg, "A new technique for tracking the global maximum power point of PV arrays operating under partial-shading con-ditions," *IEEE J. Photovolt.*, vol. 2, no. 2, pp. 184–190, Apr. 2012.

[11] Y. Li, T. Lee, and F. Z. Peng, "A hybrid control strategy for photo-voltaic simulator," in *Proc. 24th IEEE Appl. Power Electron. Conf.*, 2009, pp. 899–903.

[12] S. Chattopadhyay and S. Das, "A digital current-mode control technique for DC-DC converters," *IEEE Trans. Power Electron.*, vol. 21, no. 6, pp. 1718–1726, Nov. 2006.

[13] J. Zhao and J. W. Kimball, "A digitally implemented photovoltaic sim-ulator with a double current mode controller," in *Proc. 27th IEEE Appl. Power Electron. Conf.*, 2012, pp. 53–58.

[14] W. Zhang and J. W. Kimball, "DC-DC converter based photovoltaic sim-ulator with a double current mode controller," in *Proc. 2016 IEEE Power Energy Conf.*, 2016.

[15] J. Chen, A. Prodic, R. W. Erickson, and D. Maksimovic, "Predictive digital current programmed control," *IEEE Trans. Power Electron.*, vol. 18, no. 1, pp. 411–419, Jan. 2003.

[16] Y. S. Lai and C. A. Yeh, "Predictive digital-controlled converter with peak current-mode control and leading-edge modulation," *IEEE Trans. Ind. Electron.*, vol. 56, no. 6, pp. 1854–1863, Jun. 2009.

Weichao Zhang received the B.S. and M.S. de-grees in electrical and computer engineering from the Missouri University of Science and Technology, Rolla, MO, USA, in 2014 and 2017, respectively.

He is currently working as an RAN Engineer in AT&T, Tustin, CA, USA. His research interests in-clude control of power electronic converters, photo-voltaic applications, and power systems.

Jonathan W. Kimball (M'96—SM'05) received the B.S. degree in electrical and computer engineering from Carnegie Mellon University, Pittsburgh, PA, USA, in 1994, the M.S. degree in electrical engi-neering from the University of Illinois at Urbana-Champaign, Champaign, IL, USA, in 1996, and the Ph.D. degree in electrical and computer engineering from Illinois in 2007.

From 1996 to 1998, he worked for Motorola, Phoenix, AZ, designing IGBT modules for indus-trial applications. He, then, joined Baldor Electric, Fort Smith, AR, where he designed industrial adjustable speed drives ranging 1–150 hp. In 2003, he returned to Illinois as a Research Engineer (later a Senior Research Engineer). Later in 2003, he cofounded SmartSpark Energy Systems, Inc., Champaign, IL, and served as Vice President of engineering. He joined Missouri S&T (formerly the University of Missouri-Rolla) in 2008 as an Assis-tant Professor, and was promoted to Associate Professor (with tenure) in 2014. He is currently a Dean's Scholar of the Missouri Science and Technology Col-lege of Engineering and Computing, Rolla, MO, USA.

Dr. Kimball is a member of Eta Kappa Nu, Tau Beta Pi, and Phi Kappa Phi. He is a licensed Professional Engineer in the State of Illinois. He has served as the General Chair of the IEEE Applied Power Electronics Conference in 2017.